NeuroImage 231 (2021) 117825

Contents lists available at ScienceDirect

NeuroImage

journal homepage: www.elsevier.com/locate/neuroimage

Spatiotemporal dynamics of nonhuman primate white matter development during the first year of life

Nakul Aggarwal[a,1,*], Jason F. Moody[b,1], Douglas C. Dean, III[b,c,d], Do P.M. Tromp[a], Steve R. Kecskemeti[d], Jonathan A. Oler[a], Andy L. Alexander[a,b,d], Ned H. Kalin[a]

[a] Department of Psychiatry, University of Wisconsin-Madison, 6001 Research Park Boulevard, Madison, WI 53719, United States
[b] Department of Medical Physics, University of Wisconsin-Madison, 1111 Highland Avenue, Madison, WI 53705, United States
[c] Department of Pediatrics, University of Wisconsin-Madison, 600 Highland Avenue, Madison, WI 53792, United States
[d] Waisman Center, University of Wisconsin-Madison, 1500 Highland Avenue, Madison, WI 53705, United States

ARTICLE INFO

Keywords:
Diffusion tensor imaging
Neonatal neurodevelopment
Nonhuman primate
Longitudinal imaging
White matter

ABSTRACT

White matter (WM) development early in life is a critical component of brain development that facilitates the coordinated function of neuronal pathways. Additionally, alterations in WM have been implicated in various neurodevelopmental disorders, including psychiatric disorders. Because of the need to understand WM development in the weeks immediately following birth, we characterized changes in WM microstructure throughout the postnatal macaque brain during the first year of life. This is a period in primates during which genetic, developmental, and environmental factors may have long-lasting impacts on WM microstructure. Studies in nonhuman primates (NHPs) are particularly valuable as a model for understanding human brain development because of their evolutionary relatedness to humans. Here, 34 rhesus monkeys (23 females, 11 males) were imaged longitudinally at 3, 7, 13, 25, and 53 weeks of age with T1-weighted (MPnRAGE) and diffusion tensor imaging (DTI). With linear mixed-effects (LME) modeling, we demonstrated robust logarithmic growth in FA, MD, and RD trajectories extracted from 18 WM tracts across the brain. Estimated rate of change curves for FA, MD, and RD exhibited an initial 10-week period of exceedingly rapid WM development, followed by a precipitous decline in growth rates. K-means clustering of raw DTI trajectories and rank ordering of LME model parameters revealed distinct posterior-to-anterior and medial-to-lateral gradients in WM maturation. Finally, we found that individual differences in WM microstructure assessed at 3 weeks of age were significantly related to those at 1 year of age. This study provides a quantitative characterization of very early WM growth in NHPs and lays the foundation for future work focused on the impact of alterations in early WM developmental trajectories in relation to human psychopathology.

1. Introduction

Infancy and early childhood constitute a critical period of rapid and dynamic neurodevelopment, characterized by processes that span prenatal and early postnatal phases, including synaptogenesis and myelination (Bakken et al., 2015; Bourgeois et al., 1994; Dimond et al., 2020; Gao et al., 2009; Keunen et al., 2017; Kim et al., 2020; Kostovic and Rakic, 1980; Rakic, 1985, 1972). These developmental processes provide the structural foundation for the maturation of key adaptive emotional and behavioral skills (Deoni et al., 2014; Girault et al., 2019; O'Muircheartaigh et al., 2014). A central feature of neurodevelopment is the integration of disparate brain regions and neuronal populations. In this regard, white matter (WM) – consisting primarily of myelinated axons – is important as it facilitates electrical signal transmission in the brain, resulting in finely tuned neuronal communication. Correspondingly, alterations in WM microstructure identified during childhood have been associated with some psychiatric and neurological disorders (Heng et al., 2010; Kim and Whalen, 2009; Savadjiev et al., 2014; Tromp et al., 2019). However, despite over a century of study, our understanding of WM development during the earliest phases of life is in-

---

* Corresponding author.
E-mail address: naggarwal5@wisc.edu (N. Aggarwal).
[1] Both the authors contributed equally to this work.

https://doi.org/10.1016/j.neuroimage.2021.117825
Received 25 September 2020; Received in revised form 22 January 2021; Accepted 27 January 2021

complete. This is particularly the case in relation to WM developmental patterns in the weeks immediately following birth. Establishing a nuanced understanding of the early postnatal trajectories of WM maturation across the brain is essential for characterizing the ontogeny of the brain-wide connectivity that underlies adaptive behavioral, cognitive, and emotional responses. Such an understanding could lead to novel insights into pathophysiology of early-life psychopathology and may provide a rationale for the development of novel early treatment strategies targeting WM.

A growing body of literature has characterized WM development throughout childhood, adolescence, and adulthood (Lebel and Beaulieu, 2011). In this regard, diffusion tensor imaging (DTI) is a powerful tool for examining the microstructural properties of WM (Alexander et al., 2007; Pierpaoli and Basser, 1996). DTI uses the magnetic resonance (MR) signal attenuation resulting from diffusing water molecules to model the differential restriction of water movement throughout the brain. The primary metrics derived from DTI include fractional anisotropy (FA), mean diffusivity (MD), radial diffusivity (RD), and axial diffusivity (AD), which together are sensitive to underlying microstructural changes, including myelination, axonal coherence and packing, and tissue density (Alexander et al., 2007; Jones et al., 2013).

Substantial work utilizing DTI to explore brain development has elucidated definitive patterns of WM growth across the lifespan, which have generally corroborated findings from histological studies (Brody et al., 1987; Kinney et al., 1988). *In vivo* neuroimaging studies of WM microstructure using DTI in both humans and nonhuman primates (NHPs) reveal widespread myelination and axonal organization in early childhood (indicated by increases in FA and decreases in MD and RD) (Bava et al., 2010; Brouwer et al., 2012; Giorgio et al., 2010; Hermoye et al., 2006; Kim et al., 2020; Kubicki et al., 2019; Lebel and Beaulieu, 2011; Reynolds et al., 2019). Though much of this work used cross-sectional designs, studies assessing age-related changes in WM ideally should incorporate longitudinal designs to account for the individual differences in developmental stages and trajectories (Caruana et al., 2015). With respect to the literature on WM development in infancy, most studies are either cross-sectional or limited to 1–2 early imaging timepoints (Dean et al., 2017; Dubois et al., 2008; Gao et al., 2009; Geng et al., 2012; Shi et al., 2013; Uda et al., 2015; Young et al., 2017).

NHPs are particularly valuable in characterizing the earliest phases of WM development because of their high degree of brain homology and evolutionary relatedness to humans. Thus, a better understanding of early postnatal WM development of the monkey brain could lend important insights into early WM development in humans. Also, because of these similarities, along with analogous socio-emotional behaviors, NHPs are a highly relevant animal model to study the development of adaptive and maladaptive behavioral, emotional, and cognitive processes relevant to psychopathology (Howell et al., 2019; Nelson and Winslow, 2009; Phillips et al., 2014; Zhang and Shi, 1993). Additionally, some difficulties in performing longitudinal neuroimaging studies in human infants can be overcome when using NHPs (Raschle et al., 2012).

In this study, we aimed to quantify and characterize developmental trajectories of WM during the first year of life in infant rhesus monkeys as a means to better understand WM development in human infants. This was accomplished using a longitudinal design, acquiring five diffusion MRIs over the first year of life, with four of them occurring from birth to six months of age. Regions-of-interest (ROIs), leveraged from a previously published NHP WM atlas, were delineated from 52 WM regions, constituting 18 major WM tracts. The sample consisted of 34 infant rhesus macaques (23 females, 11 males), all of which were scanned at approximately 3, 7, 13, 25, and 53 weeks of age. This age range is approximately equivalent to birth to four years old in humans (Tigges et al., 1988; Workman et al., 2013). In addition to longitudinal trajectories, we investigated the regional heterogeneity in DTI growth rates and magnitudes that may emerge very early in postnatal development. We also examined whether individual differences in WM development were maintained from very early infancy to approximately 1 year of age.

2. Methods

2.1. Subjects and housing

34 infant rhesus macaques were housed at the Wisconsin National Primate Research Center (WNPRC) in mother-infant pairs until they were weaned at approximately 6 months of age and subsequently grouped into aged matched pairs for the remainder of the study. Standard husbandry included a 12-hour light/dark cycle, two daily feeding sessions, *ad libitum* access to water, and daily enrichment. Procedures were performed using protocols approved by the University of Wisconsin Institutional Animal Care and Use Committee.

2.2. MRI acquisition and data processing

Thirty-four rhesus macaques (23 females, 11 males) were imaged with a 3T MR750 scanner (GE Healthcare, Waukesha, WI) at roughly 3, 7, 13, 25, and 53 weeks of age. Whole brain, 3D T1-weighted images were acquired with MPnRAGE (Kecskemeti et al., 2015, 2018) with 0.625 mm isotropic spatial resolution, reconstructed to 0.47 mm isotropic resolution. A 2D echo-planar, spin-echo, single-shell DTI sequence was acquired with the following parameters: TR/TE = 7000/65.8 ms, flip angle = 90°, NEX = 1, FOV = 125 mm, acquisition matrix = 128 × 128 with 0.625 partial Fourier encoding, reconstructed in-plane spatial resolution of 0.4883 mm x 0.4883 mm and a slice thickness/gap = 1.3/0 mm, 64 interleaved slices, echo-planar spacing = 884 μs, ASSET parallel imaging ($R = 2$), $b = 1000$ s/mm^2, 72 non-colinear gradient directions, 6 non-diffusion weighted images. In addition, co-planar external field maps were obtained using a dual-echo gradient echo sequence with TE1 = 7 ms and TE2 = 10 ms. Data loss of a single MPnRAGE acquisition for a single monkey occurred due to network issues.

For each scanning session, subjects were weighed, anesthetized with ketamine (20 mg/kg, IM), and given atropine sulfate (0.04 mg/kg, IM) and ketoprofen (5 mg/kg, IM). Subjects were fitted with an endotracheal tube and induced and maintained on isoflurane anesthesia (typically less than 2% isoflurane/O2). The monkeys were then placed into a custom built 8-channel receive array for NHP imaging with a built-in stereotaxic frame (Clinical MR Solutions). If it was necessary, approved isotonic fluids were administered before, during, or after scanning to maintain blood glucose levels.

The structural MPnRAGE images for each subject were iteratively spatially normalized with non-linear, diffeomorphic registration using Advanced Normalization Tools (ANTs) software (Avants et al., 2008) to produce 34 within-subject (across time) templates. The same methodology was then implemented to co-register all 34 subject specific templates to produce a final, time-averaged, population template. After correcting the raw diffusion images for noise (Tournier et al., 2019), Gibbs ringing (Tournier et al., 2019), susceptibility-induced distortions (using the external field maps), and eddy currents (Andersson and Sotiropoulos, 2016), diffusion tensors were estimated with RESTORE (Chang et al., 2005) using Diffusion Imaging in Python (DIPY) software (Garyfallidis et al., 2014). Prototypical DTI parameter maps of fractional anisotropy (FA), mean diffusivity (MD), radial diffusivity (RD), and axial diffusivity (AD) were calculated in native space and subsequently warped to our population template with non-linear, symmetric, diffeomorphic registration using ANTs (Fig. 1).

A publicly available WM ROI atlas (UW-DTIMAC271) (Adluru et al., 2011; Zakszewski et al., 2014) of young rhesus macaques was also warped to our population template with non-linear, symmetric, diffeomorphic registration using ANTs, visually assessed for alignment, and after excluding ROIs that were poorly aligned, we selected 52 total WM ROIs for analysis (Fig. 2). DTI metrics from subgroups of these ROIs

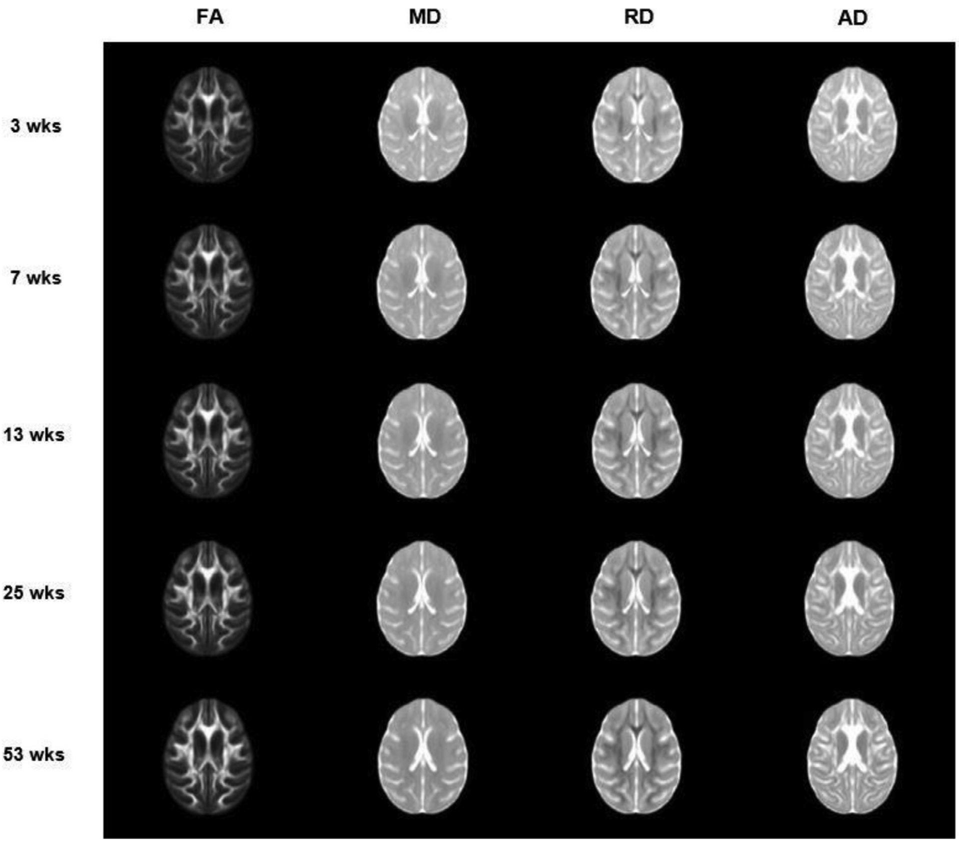

Fig. 1. From right to left: Axial views of average FA, MD, RD, and AD parameter maps for all 34 rhesus monkeys in the population template space; shown from top to bottom at 3, 7, 13, 25, and 53 weeks of age.

Table 1
Table of the 18 WM tracts organized by fiber type.

Association Tracts	Commissural Tracts	Projection Tracts	Brainstem Tracts
superior longitudinal fasciculus	anterior commissure	corona radiata	cerebellar peduncles
superior fronto-occipital fasciculus	corpus callosum	internal capsule	cerebral peduncles
uncinate fasciculus			medial lemniscus
sagittal striatum			medial longitudinal fasciculus
external capsule			corticospinal tract
cingulum			
stria terminalis			
posterior thalamic radiation			
fornix			

were averaged to represent 18 major WM tracts of interest. These tracts constitute an assortment of projection (2), commissural (2), association (9), and brainstem (5) pathways that span every region of the brain and represent a broad compilation of WM structures. All 52 ROIs and associated tracts are delineated in Table 1 and Supplemental Tables 1–3. Additionally, a WM mask of our population template was computed with FMRIB's Automated Segmentation Tool (FAST) (Zhang et al., 2001), so that changes in FA, MD, RD, and AD could be assessed globally. This mask was also applied to our warped WM atlas for the purposes of restricting subsequent analysis to WM voxels.

2.3. Developmental trajectories and nonlinear regression

For each subject and time point, average values of FA, MD, RD, and AD were extracted from the 18 WM tracts of interest and then used to construct longitudinal trajectories. Using MATLAB software, non-linear regression (via sum of squared errors [SSE] minimization) was implemented to fit these trajectories to a range of plausible growth models. Candidate models included linear, quadratic, logarithmic, exponential, and Gompertz functions (Table 2). Information criterion parameters, including Akaike Information Criterion (AIC) and Bayesian Information Criterion (BIC), as well as sum of squared errors (SSE), were calculated to evaluate the goodness of fit for each proposed model in all WM voxels delineated by our WM mask. Model testing demonstrated that a logarithmic growth model fit best with respect to FA, MD, and RD, as defined below:

$$FA\,(or\,MD,\,RD,\,AD) = A * ln(GestAge) + B \tag{1}$$

In this model, the parameter ***A*** represents the rate of change of FA (MD/RD/AD) and the parameter ***B*** represents the magnitude of FA (MD/RD/AD) at 1 week of gestational age. AD was best modeled by a quadratic function, followed closely by logarithmic and linear functions.

2.4. Linear mixed-effects modeling

After establishing the best fit for all four DTI parameters, we quantified their growth over time within the framework of a linear mixed-effects (LME) model to achieve a more robust and complete characterization of early WM development. For all 18 WM tracts, we modeled FA, MD, RD, and AD trajectories with this general form:

$$\begin{aligned} &FA\,(or\,MD,\,RD,\,AD) = \beta0 + \beta1 * \ln(GestAge) \\ &+\beta2 * Sex + \beta3 * \left(\ln(GestAge)\cdot Sex\right) + \mu0 + \mu1 * \ln(GestAge) + \varepsilon \end{aligned} \tag{2}$$

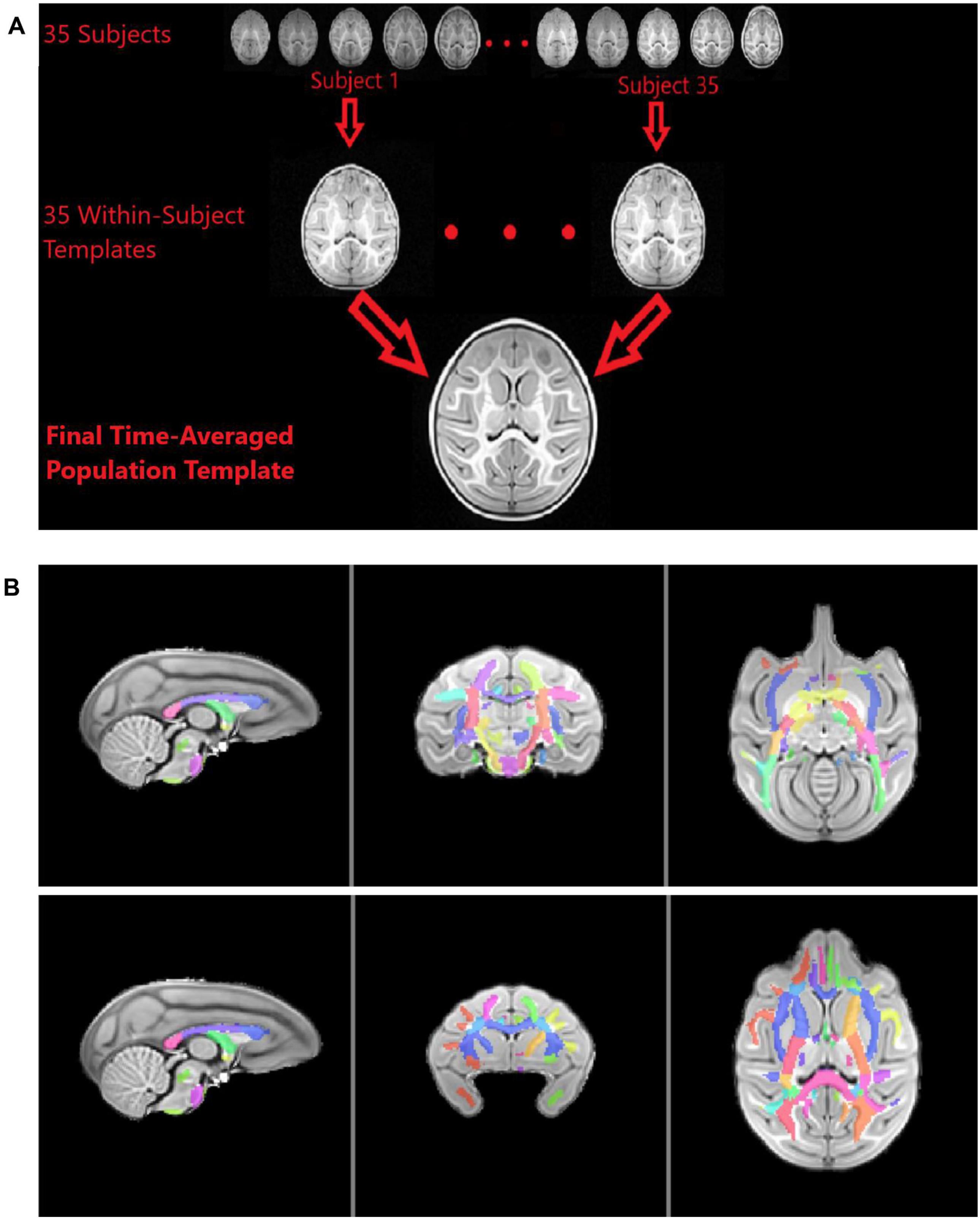

Fig. 2. (A) Schematic illustrating the population template formation process. The top row depicts the 5 MPnRAGE scans of each rhesus monkey subject. For each subject, these 5 scans are co-registered with ANTS to produce a within-subject template (middle row). Then, all 35 of these within-subject templates are co-registered with ANTS to generate a final (temporally-averaged) population template (bottom row). (B) Views of the UW-DTIMAC271 rhesus WM Atlas overlaid onto our population template. Sagittal (left), coronal (middle), and axial (right). (C) A 3D rendering of the UW-DTIMAC271 WM Atlas warped onto the population template.

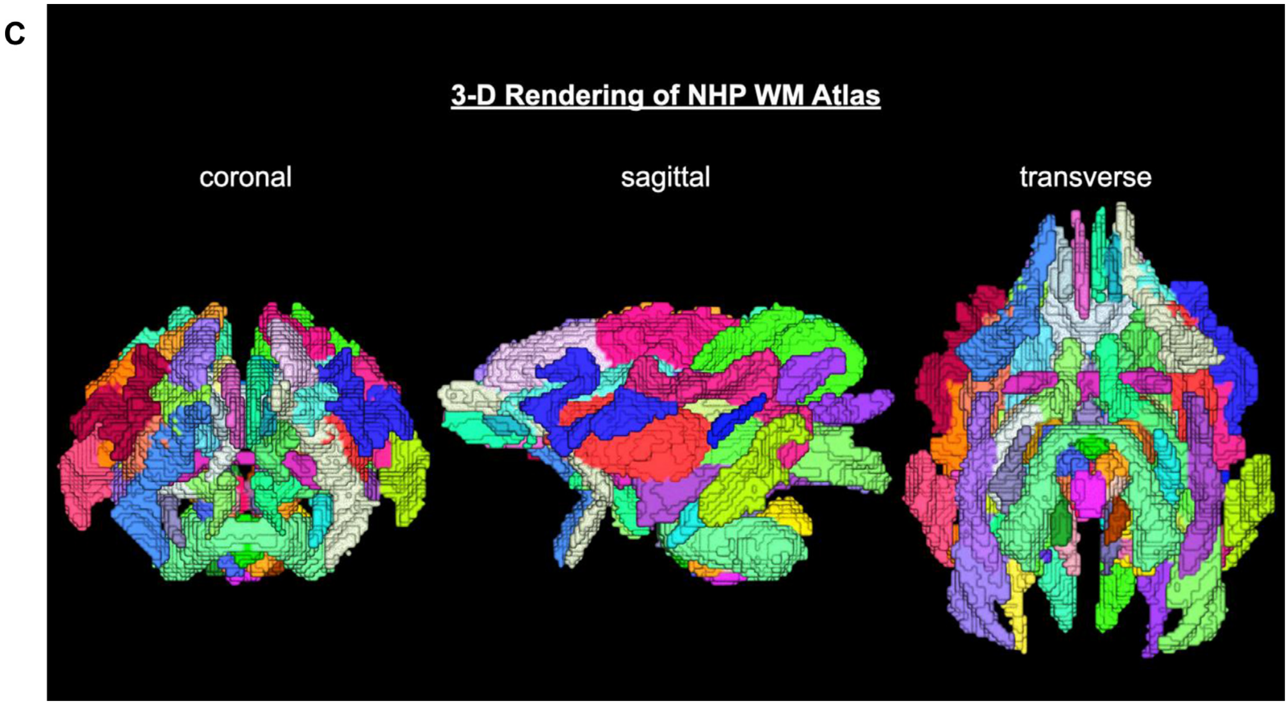

Fig. 2. Continued

Table 2
The proposed DTI trajectory models in global white matter (GWM). Akaike Information Criterion (AIC), Bayesian Information Criterion (BIC), and Sum of Squared Error (SSE) values are shown. The metrics with the lowest values are bolded for each DTI parameter, indicating that the logarithmic model provides the best fit for FA, MD, and RD, while the quadratic model provides the best fit for AD.

Non-Linear Curve-Fitting of DTI Trajectories in Global White Matter						
	Metric	$A(GestAge) + B$	$A(GestAge^2) + B(GestAge) + C$	$Aln(GestAge) + B$	$A + Be^{C*GestAge}$	$Ae^{Be^{C}*GestAge}$
FA	AIC	−1398.75	−1432.9	**−1434.31**	−1184.47	−1218.67
	BIC	−1392.48	−1424.9	**−1426.67**	−1175.06	−1209.17
	SSE	0.047	0.036	**0.036**	0.155	0.173
MD	AIC	−1249.06	−1278.49	**−1288.89**	−1069.87	−1070.89
	BIC	−1242.79	−1269.08	**−1282.62**	−1060.46	−1060.54
	SSE	0.107	0.089	**0.085**	0.303	0.303
RD	AIC	−1218.97	−1242.70	**−1266.36**	−1012.39	−1012.4
	BIC	−1212.70	−1233.39	**−1260.09**	−1002.99	−1003.1
	SSE	0.128	0.1	**0.097**	0.425	0.425
AD	AIC	−1228.97	**−1292.58**	−1249.37	−1163.78	−1163.77
	BIC	−1222.70	**−1283.17**	−1243.10	−1154.36	−1154.33
	SSE	0.120	**0.082**	0.107	0.175	0.175

LME models allow for precise and unbiased effect estimates by accounting for repeated within-subject measures. Our model is linear with respect to the natural log of gestational age at scan (GestAge) and also includes the Sex (male or female), and the interaction between ln(GestAge) and Sex as covariates. In the equation denoted above, we estimate four fixed effects: $\beta 0$ refers to the overall model intercept; $\beta 1$ refers to the main effect of GestAge (log-transformed) – our primary variable of interest; $\beta 2$ refers to the main effect of Sex; and $\beta 3$ refers to the interactive effect of GestAge and Sex. To account for the repeated longitudinal within-subject measurements, we also estimate two random effects: $\mu 0$ refers to the by-subject random intercept and $\mu 1$ refers to the by-subject random effect (slope) of GestAge. For each of 34 monkeys, we calculated $\mu 0$ *and* $\mu 1$ for each tract. Lastly, ε refers to the variance of the model residuals. In total, we generated 72 different LME models, one for each DTI parameter (FA, MD, RD, AD) in each of 18 WM tracts (18 tracts * 4 DTI parameters). All LME modeling was performed using the lme4 package in R (Bates et al., 2015).

To investigate and control for the impact of total brain volume on FA trajectories, we conducted a supplementary analysis using an alternative LME model that also included a within-subject measure of total brain volume as a covariate but was otherwise identical to the one described above. To this end, total brain volumes were extracted from the MPnRAGE structural images for each animal and timepoint using FSL software (Jenkinson et al., 2012).

2.5. Rate of change curves

To quantify how rapidly FA, MD, RD, and AD change throughout the developing macaque brain, we calculated rates of change of all four

DTI metrics ($\frac{dFA}{dGestAge}$, $\frac{dMD}{dGestAge}$, $\frac{dRD}{dGestAge}$, and $\frac{dAD}{dGestAge}$, respectively) by taking the derivative of our mixed-effects model with respect to GestAge for each WM tract. The interactive effect between GestAge and Sex ($\beta 3$) was dropped, as it was insignificant in the LME models for all 18 tracts. This produced an equation of the following form for each of the 18 WM tracts, describing the speed at which FA, MD, RD, and AD change with age in each tract:

$$\frac{dFA}{dt}\left(or\frac{dMD}{dt}, \frac{dRD}{dt}, \frac{dAD}{dt}\right) = \frac{\beta 1}{GestAge} \tag{3}$$

The rate of change of each tract, for each of the four DTI parameters (FA, MD, RD, AD), was estimated by substituting ages ranging from 3 to 52 weeks (in one-week increments) into this equation.

2.6. Individual differences in DTI metrics across time

To assess whether individual differences in these DTI parameters were maintained across time, we computed Pearson correlations for individual measures of each animal between 3 weeks of age (timepoint 1) and 1 year of age (timepoint 5).

2.7. Rank order analysis and clustering of raw DTI trajectories

Next, to delineate regional differences in WM status and development across the postnatal brain, we first ranked the magnitudes of the intercept ($\beta 0$) and slope ($\beta 1$) terms from the LME models generated for each WM tract in descending order. Next, we implemented k-means clustering of the raw FA, MD, RD, and AD trajectories corresponding to the 18 WM tracts. We chose to partition the data into 4 clusters. While determining the optimal number of clusters generated from a k-means algorithm is largely subjective, our cluster selection was based on analysis of multiple k-means clustering criteria and cluster interpretability (Supplemental Figure 6). In order to validate the consistency of these results, we performed a split-half reliability analysis – partitioning the data into two random halves (n = 17 each) and conducting k-means clustering on each subset. All clustering and statistical procedures were performed using the kml software package in R (a k-means clustering algorithm specifically designed for clustering longitudinal trajectories) (Genolini et al., 2015).

2.8. Data availability

We intend to share all project data following completion of all relevant study analyses and anticipate uploading raw data to NeuroVault (https://neurovault.org/) in late 2021. In the interim, imaging data, along with the code used for these studies, may be able to be shared with interested parties upon request by contacting the corresponding author.

3. Results

3.1. DTI metrics exhibit robust logarithmic growth over the first year of life

The fundamental aim of this study was to establish a quantitative framework for characterizing global and regional WM development across the infant macaque brain over the first year of life. To that end, we evaluated WM trajectories of FA, MD, RD, and AD extracted from 18 WM tracts (Fig. 3). To establish the growth model that best fit these data, a number of candidate models were fit to the raw data trajectories and compared with three widely used curve-fitting metrics (namely, SSE, AIC, and BIC). We found that a 2-parameter logarithmic model was the best fit for FA, MD, and RD trajectories. A quadratic model was the best fit for AD trajectories, though a 2-parameter logarithmic model also demonstrated an adequate fit. Table 2 provides the SSE, AIC, and BIC values for each of the tested models.

After establishing the validity of using natural log-transformed age for each DTI parameter, we next accounted for individual differences as well as sex and gestational development in an LME model to test whether log-transformed gestational age significantly predicted changes in DTI parameters over time. Results demonstrated that for all 18 tracts, the log-transformed GestAge term ($\beta 1$) remained significant in predicting changes in FA, MD, and RD over time (Bonferroni corrected $p_{corrected}<0.05$). In relation to AD, $\beta 1$ remained significant for 12 of 18 tracts (67%) (Bonferroni corrected $p_{corrected}<0.05$). Because GestAge is correlated with brain volume and DTI parameters, and because brain volume and DTI parameters are frequently correlated, we performed this analysis to disentangle the unique contributions of GestAge on DTI parameters – independent of total brain volume. In our supplementary LME analysis of FA trajectories that additionally covaried for total brain volume, the ln(GestAge) term ($\beta 1$) was still highly significant in all 18 tracts, accounting for unique variance beyond that accounted for by total brain volume (Bonferroni corrected $p_{corrected}<0.05$). We illustrate the effect of total brain volume on whole brain FA (calculated by averaging all 18 tracts) in Supplementary Figure 7.

3.2. WM development is rapid over the first 10 weeks of life and slows dramatically by 25 weeks

Qualitatively, the logarithmic WM growth trajectories of FA, MD, and RD showed remarkably fast growth in the few weeks immediately following birth. To quantitatively characterize the rapid nature of WM development over the first year of life, we took the derivative of our LME equations with respect to age for 18 WM tracts to produce rate of change estimates for FA, MD, RD, and AD (Fig. 4).

Rate of change curves for FA, MD, and RD exhibit the same two notable features. First, WM appears to develop extremely rapidly over the first 10 weeks of life across the entire brain. Visually, this is documented by the steep slopes occurring over the first 10 weeks. Quantitatively, this observation manifests in that the magnitudes of dFA/dt, dMD/dt, and dRD/dt for all 18 tracts drop to less than 25% of their initial values by 10 weeks of age. Secondly, WM maturation begins to slow substantially by approximately 25 weeks (~6 months). We note that the corresponding magnitudes of the rates of change for each DTI metric are less than 10% of their initial values in all tracts by 25 weeks of age and change very gradually thereafter.

3.3. Individual differences in WM metrics across the first year of life

Correlations between subject-level FA, MD, RD, and AD measurements from the 18 WM tracts at the earliest and latest timepoints reveal that a monkey's relative WM status at 3 weeks old is meaningfully related to its developmental state at 1 year, especially with regard to FA. Specifically, 16 of 18 FA tract correlations, 8 of 18 RD tract correlations, 5 of 18 MD tract correlations, and 4 of 18 AD tract correlations were significant after correcting for multiple comparisons (Table 3). Of note, at an uncorrected threshold ($p_{uncorrected}<0.05$), 17 of 18 FA correlations, 15 of 18 RD correlations, 14 of 18 MD correlations, and 13 of 18 AD correlations are significant. Graphs of the FA and MD correlations across time are depicted in Fig. 5, and corresponding graphs for RD and AD are shown in Supplemental Figure 4.

3.4. Regional asynchrony during very early WM development

Results from k-means clustering of FA, MD, and RD trajectories and rank ordering of LME parameters ($\beta 0$ and $\beta 1$) for the 18 WM tracts delineate regional differences in WM microstructure changes over time (Fig. 6 and Supplemental Figure 5). Based on multiple k-means clustering criteria (Genolini et al., 2015), four clusters were selected in the clustering analysis for each DTI metric. With respect to FA, we find prominent medial-to-lateral and posterior-to-anterior progression of WM growth.

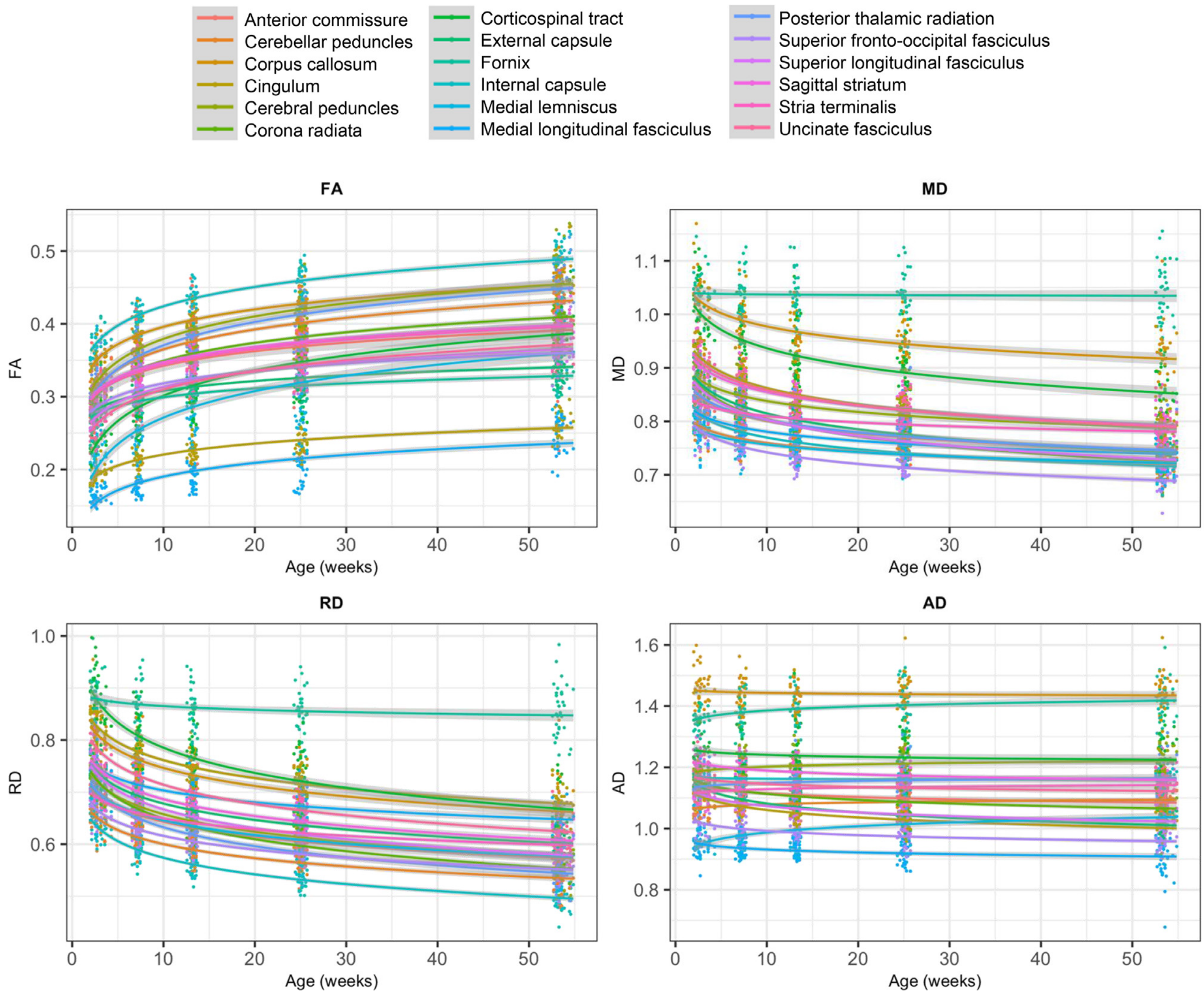

Fig. 3. Average trajectories of FA, MD, RD, and AD for 18 WM tracts. The lines represent logarithmic fits for each tract.

Table 3
R^2 values (along with corresponding p-values) between 3 weeks and 1 year for each WM tract (shown in Fig. 5). Significant R^2 values ($p_{corrected}$ <0.05) are bolded.

Tract	FA	MD					RD			AD		
	R^2	p	p-corr	R^2	p	p-corr	R^2	p	p-corr	R^2	p	p-corr
fornix	**0.599**	8.02E-08	1.44E-06	**0.249**	0.003	0.048	**0.334**	3.45E-04	6.21E-03	0.166	1.66E-02	0.30
anterior commissure	**0.804**	7.23E-13	1.30E-11	**0.270**	0.002	0.029	**0.591**	1.10E-07	1.98E-06	**0.609**	5.25E-08	9.45E-07
cerebellar peduncles	**0.360**	1.75E-04	3.15E-03	0.132	0.035	0.628	0.214	0.006	0.105	0.115	0.050	0.895
corpus callosum	**0.444**	1.69E-05	3.04E-04	**0.441**	1.84E-05	3.31E-04	**0.437**	2.08E-05	3.74E-04	**0.458**	1.11E-05	2.00E-04
corticospinal tract	**0.403**	5.47E-05	9.85E-04	0.040	0.256	4.608	0.141	0.028	0.513	0.005	0.679	12.215
medial lemniscus	**0.306**	6.97E-04	1.26E-02	0.200	0.008	0.143	0.137	0.031	0.556	0.049	0.210	3.778
cerebral peduncles	**0.455**	1.23E-05	2.21E-04	0.169	0.016	0.284	**0.263**	0.002	0.035	0.174	0.014	0.255
internal capsule	**0.455**	1.20E-05	2.16E-04	0.194	0.009	0.164	**0.287**	1.10E-03	1.98E-02	0.204	7.40E-03	1.33E-01
corona radiata	**0.414**	4.05E-05	7.29E-04	0.149	0.024	0.430	0.177	0.013	0.240	0.199	0.008	0.148
sagittal striatum	**0.450**	1.40E-05	2.52E-04	**0.364**	1.57E-04	0.003	**0.378**	1.09E-04	1.96E-03	**0.391**	7.67E-05	1.38E-03
external capsule	**0.300**	8.09E-04	1.46E-02	0.155	0.021	0.386	0.137	0.031	0.565	0.230	0.004	0.073
cingulum	**0.426**	2.86E-05	5.15E-04	0.088	0.088	1.580	0.187	0.011	0.190	0.035	0.293	5.270
stria terminalis	0.187	1.06E-02	0.19	0.145	0.026	0.474	0.097	0.072	1.301	0.211	0.006	0.114
superior longitudinal fasciculus	**0.477**	6.14E-06	1.11E-04	0.149	0.024	0.435	0.189	0.010	0.183	0.233	0.004	0.069
superior fronto-occipital fasciculus	**0.505**	2.48E-06	4.46E-05	0.043	0.240	4.320	0.106	0.061	1.093	0.052	0.195	3.510
uncinate fasciculus	**0.268**	1.72E-03	3.09E-02	0.225	0.005	0.082	**0.367**	1.47E-04	2.64E-03	0.149	2.42E-02	0.44
medial longitudinal fasciculus	0.095	0.075	1.357	0.005	0.687	12.366	0.014	0.501	9.018	0.000	0.920	16.553
posterior thalamic radiation	**0.464**	9.22E-06	1.66E-04	**0.562**	3.31E-07	5.96E-06	**0.451**	1.36E-05	2.45E-04	**0.670**	3.31E-09	5.96E-08
Average of Significant R^2	**0.446**			**0.377**			**0.388**			**0.532**		

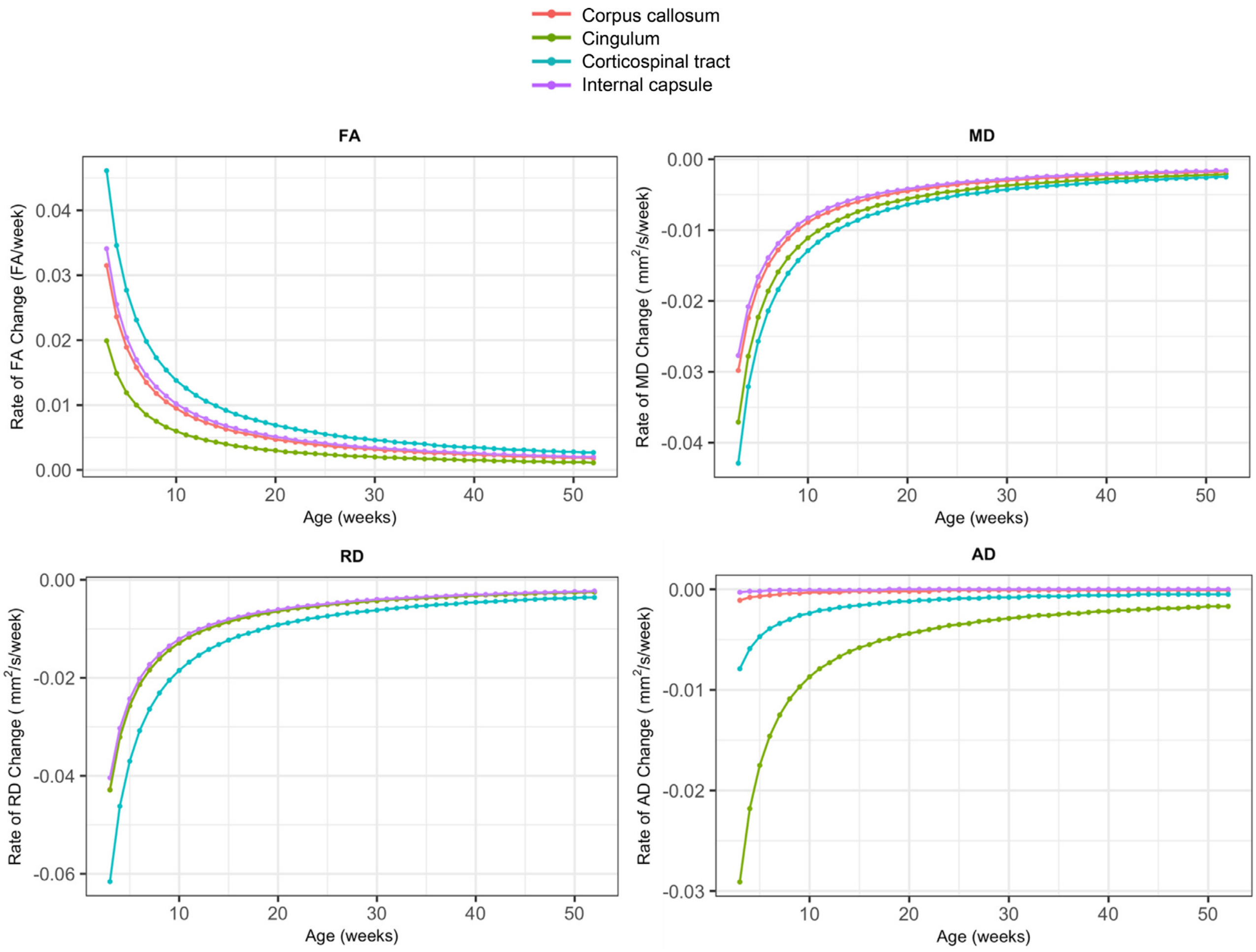

Fig. 4. Predicted rate of change curves for FA, MD, RD, and AD estimated for 4 select WM tracts. Curves for FA, MD, and RD exhibit rapid changes over the first 10 weeks of life, followed by a characteristic decrease in rates, whereby rates in all tracts fall to less than 10% of their initial magnitudes by 25 weeks of age.

In relation to FA, Cluster 1, which consists of regions that develop earliest in life, is comprised of the cerebral peduncles, internal capsule, corpus callosum, and posterior thalamic radiation. Cluster 2 includes the anterior commissure, cerebellar peduncles, corona radiata, sagittal striatum, and stria terminalis. Cluster 3 contains the corticospinal tract, external capsule, fornix, medial lemniscus, superior fronto-occipital fasciculus. superior longitudinal fasciculus, and the uncinate fasciculus. Finally, Cluster 4 consists of the cingulum and medial longitudinal fasciculus. Note that these cluster compositions were largely consistent in a split-half reliability analysis (FA: $r = 0.97$; MD: $r = 0.86$; RD: $r = 0.92$; AD: $r = 0.91$) (Supplemental Table 8).

We note that the clustering results for MD and RD differed considerably from those for FA but were largely consistent with each other. With respect to both MD and RD, as seen in Fig. 6 and Supplemental Figure 5, Clusters 1 and 2 share 12 tracts. Cluster 3 shares 2 tracts, and Cluster 4 consists solely of the fornix for both metrics. Comparison of the rank orders of $\beta 0$ and $\beta 1$ to k-means clusters of FA, MD, RD, and AD trajectories suggests that regional differentiation in the first year is primarily driven by the initial magnitudes of DTI metrics.

4. Discussion

This study characterizes, in the NHP, the *in vivo* development of WM microstructure during the earliest weeks of postnatal life throughout the first year. Of particular importance is the present study's focus on the developmental changes during the first six months. While a large body of work has examined early WM growth in humans and NHPs (Dean et al., 2014a; Dean et al., 2014b; Huang et al., 2006; Kim et al., 2020; Malkova et al., 2006), few studies have offered an in-depth view of WM proliferation in the days immediately following birth. Here, using a longitudinal within-subjects design, we leverage a previously published rhesus WM atlas to study 18 WM tracts across the brain and model their spatiotemporal dynamics beginning at 3 weeks of age and continuing through 53 weeks.

In general, the trajectory analyses with DTI metrics used here demonstrate a logarithmic pattern in the development of WM across the first year of life. Individual differences in WM microstructure are evident as early as 3 weeks postnatally, and these individual differences persist, as DTI values at 3 weeks are significantly correlated with those at 53 weeks. Finally, we provide evidence of regional differentiation in WM development in the first few weeks of life that aligns with previous literature outlining a posterior-to-anterior and medial-to-lateral maturational gradient.

WM maturation in early childhood, most commonly indexed by FA, is thought to be driven by progressive myelination and increased axonal coherence (Friedrich et al., 2020). An extensive body of work in both humans and NHPs has documented this pattern of rapid growth in infancy and early childhood, followed by stable linear growth through adolescence (Giorgio et al., 2010; Kubicki et al., 2019; Scott et al., 2015). Consistent with the findings of rapid synaptogenesis occurring in the earliest months of postnatal life in primates (Bourgeois et al., 1994; Rakic, 1985; Rakic, 1972), our results add to the current understanding specifically of WM development by establishing WM trajectories from birth to 1 year of age in rhesus monkeys, which is generally equivalent to birth to four

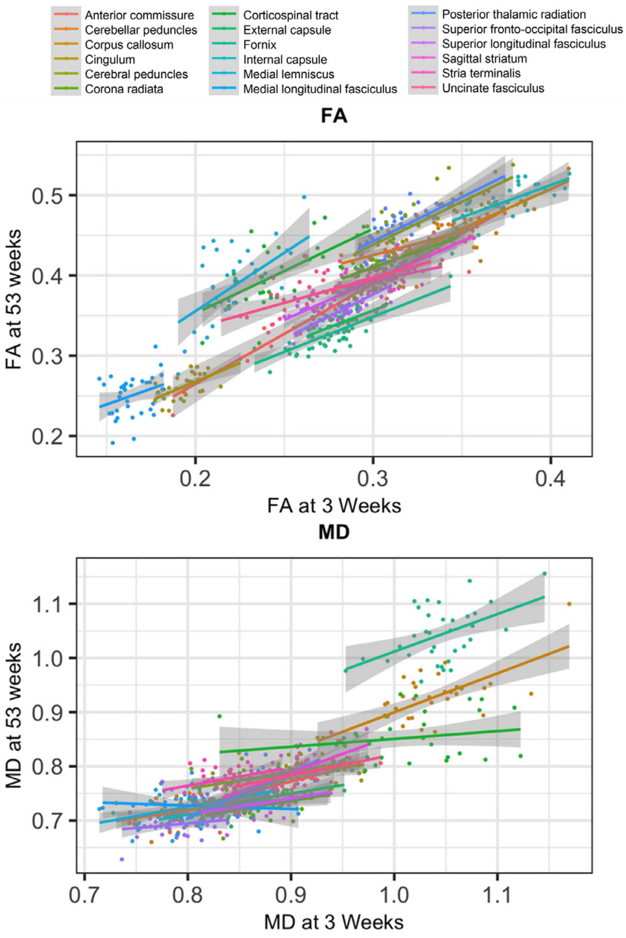

Fig. 5. Within-subject individual differences in DTI metrics between 3 weeks and 1 year of age for FA and MD. Corresponding plots for RD and AD are shown in Supplemental Figure 4.

years of age in humans. Linear mixed-effects modeling of the effect of gestational age on FA, MD, and RD revealed robust, statistically significant, logarithmic growth across all WM tracts during the first year of life (Fig. 3 and Table 2). Moreover, as demonstrated in a supplemental analysis that included total brain volume as an additional covariate, gestational age accounted for distinct variance in FA, separate from that related to total brain volume. This suggests that observed increases in FA during infancy are indeed reflective of developmental changes in WM microstructure, not simply macrostructural changes related to brain size.

In comparison to FA, MD, and RD, logarithmic growth for AD was observed in only 12 of 18 tracts examined. Additionally, AD trajectories throughout the brain were relatively flat, with most regions exhibiting small decreases in AD and others exhibiting small increases (Fig. 3). The small variations and lack of a universal direction in our AD growth curves are consistent with other reports of longitudinal trajectories in AD assessed early in life in humans and NHPs (Bava et al., 2010; Giorgio et al., 2008; Krogsrud et al., 2016; Lebel and Beaulieu, 2011; Lebel et al., 2008; Moura et al., 2016; Sadeghi et al., 2013; Scherf et al., 2014; Simmonds et al., 2014).

The first 25 weeks of NHP life is characterized by rapid growth across all WM tracts. Our region-specific rate of change models offer a precise quantitative assessment of this phenomenon (Fig. 4). We observed the highest rates of immediate postnatal change in posterior, medial, and brainstem regions of WM, including the medial lemniscus, corticospinal tract, the cerebral and cerebellar peduncles, and the posterior thalamic radiation, suggesting an intense and early period of accelerated WM development in posterior and medial regions occurring during the first year of life.

More broadly, we find that the rates of change in FA, MD, and RD for all WM tracts are highest at the first timepoint and then precipitously decline, falling below 25% of their initial rates by 10 weeks of age (Fig. 4). By 25 weeks of age, rates of change in FA, MD, and RD drop to less than 10% of their initial values. By 53 weeks, these rates fall to approximately 5% of initial values. These findings, along with reports of DTI metrics in older animals, suggest that the majority of WM growth is complete by 25 to 53 weeks of age (equivalent to 2–4 years in humans). Undoubtedly, WM development in the primate brain continues to occur, but the intervals of growth during later childhood, adolescence, and early adulthood unfold on a scale that is an order of magnitude smaller than the changes observed in the first months of life (Lebel and Beaulieu, 2011). Our results suggest that the first few of weeks of life is a critical period in relation to WM growth and a time of increased vulnerability to the potential impact of adverse environments and stress.

Our longitudinal dataset afforded us the opportunity to assess whether individual differences in WM microstructure were maintained across the first year of life, which cannot be accomplished by cross-sectional and accelerated longitudinal designs. The few reports relevant to this question have been performed in humans, but have only used a maximum scanning interval of up to five weeks (Bonekamp et al., 2007; Merisaari et al., 2019). Here, we show that individual differences in WM DTI metrics assessed at 3 weeks of age are related to those at approximately 1 year of age (Fig. 5). This finding was particularly robust in relation to FA, where in 16 of 18 bilateral tracts, FA at 3 weeks of age was significantly correlated to FA at 1 year. With respect to MD and RD, this relationship was only significant for select tracts (mainly prominent projection fibers and medial tracts), including the corpus callosum, internal capsule, anterior commissure, and fornix. Additionally, we note that the correlations between DTI metrics at 3 weeks and 1 year are generally modest (Table 3), highlighting individual variability in WM development that can be influenced by experiential and genetic factors.

Decades of histological, anatomical, and imaging studies in humans and NHPs have repeatedly identified canonical patterns of WM maturation across the brain. Broadly speaking, WM development progresses in the posterior-to-anterior and medial-to-lateral directions (Brody et al., 1987; Dean et al., 2014a; Kinney et al., 1988; Krogsrud et al., 2016; Lebel and Deoni, 2018). Additionally, among the three categories of WM bundles, projection and commissural tracts develop first, followed by association tracts (Giorgio et al., 2010; Lebel and Beaulieu, 2011; Simmonds et al., 2014). This translates into the occipital, cerebellar, internal capsule, corpus callosum, and brainstem WM exhibiting heightened development very early in life, while bundles including the uncinate fasciculus, cingulum, and fornix mature relatively late. It is likely that the maturation of tracts carrying fibers that subserve foundational sensory processing, autonomic functions, and inter-hemispheric coordination occurs earliest because they are essential to basic survival behaviors. On the other hand, tracts carrying fibers that mediate higher-order integrative and executive function, fine motor movement, and emotional regulation are less essential in the early postnatal phases of life in primates, while under the direct care of a parent. This may explain why the developmental pattern of these tracts is more gradual. Employing k-means clustering designed specifically for analysis of longitudinal data, combined with rank order analysis of LME parameters, we computationally recapitulate these established gradients of WM growth in our infant NHP sample (Fig. 6). As anticipated, WM tracts with the most elevated FA measures include the cerebellar and cerebral peduncles, posterior thalamic radiation, the internal capsule, and corpus callosum. Long-range association tracts spanning the posterior-anterior axis, such as the superior fronto-occipital fasciculus and superior longitudinal fasciculus, exhibit intermediate growth, followed lastly by short-range association fibers including the uncinate fasciculus, cingulum, and fornix. These observed patterns align with findings related to WM development in human infancy and early childhood, during which medial and posterior regions exhibit consistently elevated FA values relative to lateral and anterior regions (Geng et al., 2012; Uda et al., 2015). Our demonstration that the pattern of spatiotemporal heterochronicity in rhesus monkeys is similar to that of humans suggests that this pattern of WM development is evolutionarily conserved across primate species. These results also provide strong support for clear regional differences in WM dynamics that are apparent as early as 3 weeks of age and persist into adolescence and adulthood (Krogsrud et al., 2016; Lebel and Beaulieu, 2011; Uda et al., 2015). Notably, the rank ordering of the LME model intercepts ($\beta 0$), which represent the magnitude of DTI metrics at birth in each WM tract, coincides with the cluster compositions (Fig. 6). This underscores that the genetic programming relevant to regional differences in WM development is unfolding very early in life and is likely occurring prenatally. Indeed, postmortem tissue and *in vivo* MRI studies of human fetuses in the second and third trimesters have demonstrated myelination emerging earliest in posterior and medial WM regions, including limbic structures, internal capsule, and corpus callosum (Hasegawa et al., 1992; Huang et al., 2006; Kasprian et al., 2008; Kinney et al., 1994; Zanin et al., 2011). Finally, the results presented here reflecting early life developmental trajectories are consistent with the well-known pattern of prolonged maturation that is observed for frontotemporal association tracts. Specifically, our data demonstrate relatively slower maturation of these tracts that is evident as early as 3 weeks of life.

Our study has some notable limitations. First, some caution should be used in interpreting these NHP findings in relation to humans. Because this NHP study was performed in a controlled laboratory setting, it is important to acknowledge the differences in environmental experience between the animals used in our study and that of humans, in which there is considerably more diversity in early life environmental experiences. This is particularly relevant because brain development is influenced by a host of environment-related factors, including socioeconomic status and early life stressors (Brito and Noble, 2014; Evans, 2006; Gee et al., 2013; Telzer et al., 2015). Also, because DTI metrics are an indirect reflection of WM microstructure and are influenced by various biophysical processes, caution should be used in interpreting findings related to specific structural brain changes. For example, changes in FA have been demonstrated to reflect disparities in myelination, axonal coherence, size, and density, and cellular permeability (Friedrich et al., 2020; Roberts et al., 2005). Additionally, diffusion parameters were highly correlated to whole-brain volumetric changes across the first year of life (Supplemental Figure 7), which is why we performed supplementary analyses demonstrating the unique contributions of gestational age, while controlling for total brain volume. However, this does not rule out the possibility that our results also may reflect broader macrostructural

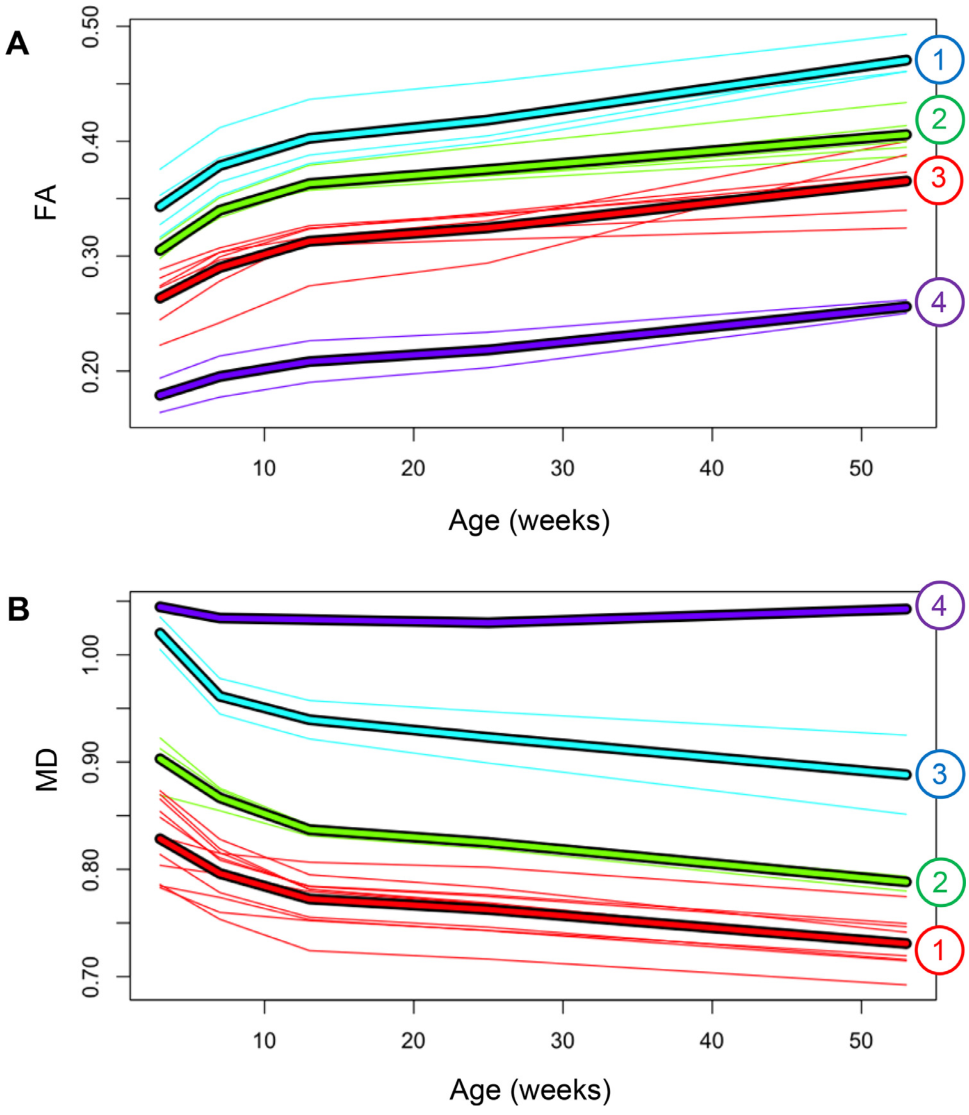

Fig. 6. Four k-means clusters derived from the trajectories of the 18 WM tracts for (A) FA and (B) MD. Cluster compositions, along with rank ordering of intercept and slope magnitudes ($\beta 0$ and $\beta 1$), for FA and MD are listed in (C), with Cluster 1 representing the tracts that develop earliest in life and Cluster 5 the later developing tracts, relative to each other. Rank order tables are color-coded by k-means cluster. Clusters and corresponding rank order tables for RD and AD trajectories are shown in Supplemental Fig. 5.

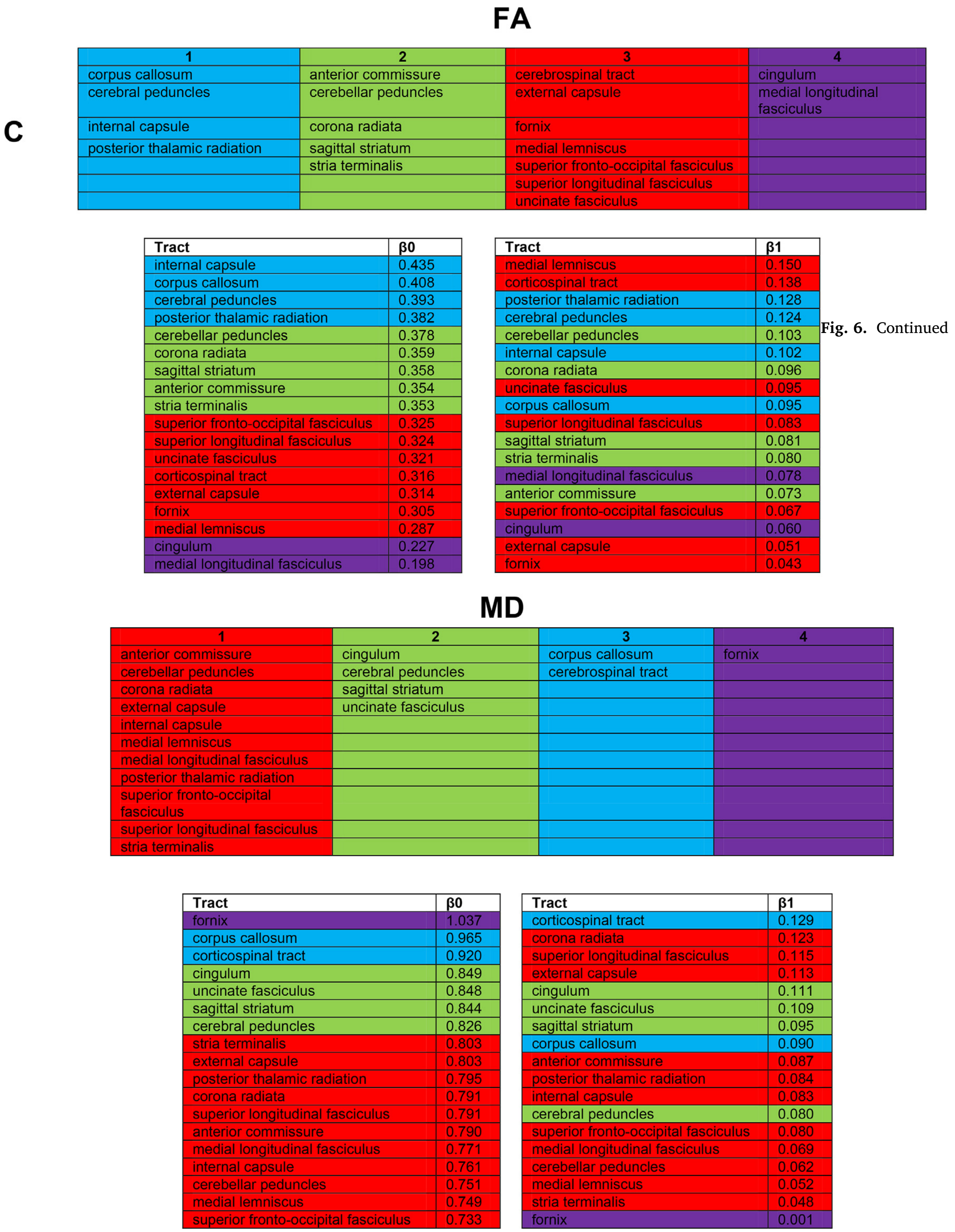

C

FA

1	2	3	4
corpus callosum	anterior commissure	cerebrospinal tract	cingulum
cerebral peduncles	cerebellar peduncles	external capsule	medial longitudinal fasciculus
internal capsule	corona radiata	fornix	
posterior thalamic radiation	sagittal striatum	medial lemniscus	
	stria terminalis	superior fronto-occipital fasciculus	
		superior longitudinal fasciculus	
		uncinate fasciculus	

Tract	β0
internal capsule	0.435
corpus callosum	0.408
cerebral peduncles	0.393
posterior thalamic radiation	0.382
cerebellar peduncles	0.378
corona radiata	0.359
sagittal striatum	0.358
anterior commissure	0.354
stria terminalis	0.353
superior fronto-occipital fasciculus	0.325
superior longitudinal fasciculus	0.324
uncinate fasciculus	0.321
corticospinal tract	0.316
external capsule	0.314
fornix	0.305
medial lemniscus	0.287
cingulum	0.227
medial longitudinal fasciculus	0.198

Tract	β1
medial lemniscus	0.150
corticospinal tract	0.138
posterior thalamic radiation	0.128
cerebral peduncles	0.124
cerebellar peduncles	0.103
internal capsule	0.102
corona radiata	0.096
uncinate fasciculus	0.095
corpus callosum	0.095
superior longitudinal fasciculus	0.083
sagittal striatum	0.081
stria terminalis	0.080
medial longitudinal fasciculus	0.078
anterior commissure	0.073
superior fronto-occipital fasciculus	0.067
cingulum	0.060
external capsule	0.051
fornix	0.043

MD

1	2	3	4
anterior commissure	cingulum	corpus callosum	fornix
cerebellar peduncles	cerebral peduncles	cerebrospinal tract	
corona radiata	sagittal striatum		
external capsule	uncinate fasciculus		
internal capsule			
medial lemniscus			
medial longitudinal fasciculus			
posterior thalamic radiation			
superior fronto-occipital fasciculus			
superior longitudinal fasciculus			
stria terminalis			

Tract	β0
fornix	1.037
corpus callosum	0.965
corticospinal tract	0.920
cingulum	0.849
uncinate fasciculus	0.848
sagittal striatum	0.844
cerebral peduncles	0.826
stria terminalis	0.803
external capsule	0.803
posterior thalamic radiation	0.795
corona radiata	0.791
superior longitudinal fasciculus	0.791
anterior commissure	0.790
medial longitudinal fasciculus	0.771
internal capsule	0.761
cerebellar peduncles	0.751
medial lemniscus	0.749
superior fronto-occipital fasciculus	0.733

Tract	β1
corticospinal tract	0.129
corona radiata	0.123
superior longitudinal fasciculus	0.115
external capsule	0.113
cingulum	0.111
uncinate fasciculus	0.109
sagittal striatum	0.095
corpus callosum	0.090
anterior commissure	0.087
posterior thalamic radiation	0.084
internal capsule	0.083
cerebral peduncles	0.080
superior fronto-occipital fasciculus	0.080
medial longitudinal fasciculus	0.069
cerebellar peduncles	0.062
medial lemniscus	0.052
stria terminalis	0.048
fornix	0.001

Fig. 6. Continued

changes. Finally, while understanding sex-related differences is important, this was not possible in our study because of the relatively low number of males that were part of the sample.

4.1. Conclusion

In summary, we present the first comprehensive DTI-based characterization of WM microstructural growth across the macaque brain during the first year of life. Specifically, we established quantitative (LME) models of FA, MD, and RD trajectories in 18 WM tracts, identifying robust logarithmic patterns in WM development throughout the brain and highlighting particularly rapid growth within the first 25 weeks of life. Leveraging a repeated-measures longitudinal design, we found distinct individual differences in DTI metrics that emerge as early as 3 weeks of age and are significantly related to individual differences at 1 year. Finally, we implemented a longitudinal k-means clustering algorithm and rank order analysis to elucidate regional differences in WM status and development. This characterization of very early WM growth in NHPs can be used for future work focused on mechanisms relevant to understanding factors modulating WM development in primates. Such studies have the potential to address how alterations in early WM developmental trajectories may contribute to the emergence of the cognitive and emotional manifestations of psychopathology.

Declaration of competing interest

At the time of writing, NHK had received honoraria from CME Outfitters and the Pritzker Consortium; serves on the advisory board of Skyland Trail; serves on the scientific advisory boards of Pritzker Neuropsychiatric Disorders Research Consortium and University of Texas at Austin Institute for Early Life Adversity Research; consults to Corcept Therapeutics; and serves as editor-in-chief of *The American Journal of Psychiatry*. The other authors report no biomedical financial interests or potential conflicts of interest.

Acknowledgments

This research was funded by the National Institutes of Health. We thank M. Styner (University of North Carolina-Chapel Hill) for providing helpful insight into analytical approaches during early stages of the project. We also thank the staffs of the Harlow Center for Biological Psychology (Marissa Riedel, Victoria Elam), Waisman Laboratory for Brain Imaging and Behavior, and Wisconsin National Primate Research Center.

Funding

This work was supported by grants from the National Institutes of Health to NHK (Grant Nos. P50-MH100031 and R01-MH081884). NA is a student in the Medical Scientist Training Program (Grant No. T32-GM008692) and the Training Program in Emotion Research (Grant No. T32-MH018931) at UW-Madison.

Research reported in this publication was also supported in part by the Office of the Director, National Institutes of Health under Award Number P51OD011106 to the Wisconsin National Primate Research Center, University of Wisconsin-Madison. This research was conducted at a facility constructed with support from Research Facilities Improvement Program grant numbers RR15459–01 and RR020141–01. The content is solely the responsibility of the authors and does not necessarily represent the official views of the National Institutes of Health.

The funding sources played no role in the conceptualization, design, execution, or analysis of any part of the study.

Credit author statement

Nakul Aggarwal – Conceptualization, Methodology, Software, Visualization, Writing-original draft, Writing-review and editing; Jason F. Moody – Conceptualization, Methodology, Software, Visualization, Writing-original draft, Writing-review and editing; Douglas C. Dean III – Methodology, Software, Writing-review and editing; Do P.M. Tromp – Methodology, Writingreview and editing; Steve R. Kecskemeti – Methodology, Software, Writing-review and editing; Jonathan A. Oler – Writing-review and editing; Andy L. Alexander – Conceptualization, Methodology, Resources, Supervision, Writing-review and editing; Ned H. Kalin – Conceptualization, Funding Acquisition, Methodology, Resources, Supervision, Writing-review and editing.

Supplementary materials

Supplementary material associated with this article can be found, in the online version, at doi:10.1016/j.neuroimage.2021.117825.

References

Adluru, N., Zhang, H., Fox, A.S., Shelton, S.E., Ennis, C.M., Bartosic, A.M., …, Alexander, A.L., 2011. A diffusion tensor brain template for rhesus macaques. Neuroimage 59 (1), 306–318. doi:10.1016/j.neuroimage.2011.07.029.

Alexander, A.L., Lee, J.E., Lazar, M., Field, A.S., 2007. Diffusion tensor imaging of the brain. Neurotherapeutics 4 (3), 1–14. doi:10.1016/j.nurt.2007.05.011.

Andersson, J.L.R., Sotiropoulos, S.N, 2016. An integrated approach to correction for off-resonance effects and subject movement in diffusion MR imaging. Neuroimage 125, 1063–1078. doi:10.1016/j.neuroimage.2015.10.019.

Avants, B.B., Epstein, C.L., Grossman, M., Gee, J.C., 2008. Symmetric diffeomorphic image registration with cross-correlation: evaluating automated labeling of elderly and neurodegenerative brain. Med. Image Anal. 12 (1), 26–41. doi:10.1016/j.media.2007.06.004.

Bakken, T.E., Miller, J.A., Luo, R., Bernard, A., Bennett, J.L., Lee, C.-K., …, Lein, E.S., 2015. Spatiotemporal dynamics of the postnatal developing primate brain transcriptome. Hum. Mol. Genet. 24 (15), 4327–4339. doi:10.1093/hmg/ddv166.

Bates, D., Mächler, M., Bolker, B., Walker, S., 2015. Fitting linear mixed-effects models using lme4. J. Stat. Softw. 67 (1). doi:10.18637/jss.v067.i01.

Bava, S., Thayer, R., Jacobus, J., Ward, M., Jernigan, T.L., Tapert, S.F., 2010. Longitudinal characterization of white matter maturation during adolescence. Brain Res. 1327, 38–46. doi:10.1016/j.brainres.2010.02.066.

Bonekamp, D., Nagae, L.M., Degaonkar, M., Matson, M., Abdalla, W.M.A., Barker, P.B., … Horská, A., 2007. Diffusion tensor imaging in children and adolescents: reproducibility, hemispheric, and age-related differences. Neuroimage 34 (2), 733–742. doi:10.1016/j.neuroimage.2006.09.020.

Bourgeois, J.-P., Goldman-Rakic, P.S., Rakic, P., 1994. Synaptogenesis in the prefrontal cortex of rhesus monkeys. Cereb. Cortex 4 (1), 78–96. doi:10.1093/cercor/4.1.78.

Brito, N.H., Noble, K.G., 2014. Socioeconomic status and structural brain development. Front. Neurosci. 8, 276. doi:10.3389/fnins.2014.00276.

Brody, B.A., Kinney, H.C., Kloman, A.S., Gilles, F.H., 1987. Sequence of central nervous system myelination in human infancy. I. An autopsy study of myelination. J. Neuropathol. Exp. Neurol. 46 (3), 283–301. doi:10.1097/00005072-198705000-00005.

Brouwer, R.M., Mandl, R.C.W., Schnack, H.G., Soelen, I.L.C.V., Baal, G.C.V., Peper, J.S., …, Pol, H.E.H., 2012. White matter development in early puberty: a longitudinal volumetric and diffusion tensor imaging twin study. PLoS One 7 (4), e32316. doi:10.1371/journal.pone.0032316.

Caruana, E.J., Roman, M., Hernández-Sánchez, J., Solli, P., 2015. Longitudinal studies. J. Thorac. Dis. 7 (11), E537–E540. doi:10.3978/j.issn.2072-1439.2015.10.63.

Chang, L.-.C., Jones, D.K., Pierpaoli, C., 2005. RESTORE: robust estimation of tensors by outlier rejection. Magn. Reson. Med. 53 (5), 1088–1095. doi:10.1002/mrm.20426.

Dean, D.C., Planalp, E.M., Wooten, W., Adluru, N., Kecskemeti, S.R., Frye, C., …, Alexander, A.L., 2017. Mapping white matter microstructure in the one month human brain. Sci. Rep. 7 (1), 9759. doi:10.1038/s41598-017-09915-6.

Dean, D.C, O'Muircheartaigh, J., Dirks, H., Waskiewicz, N., Lehman, K., Walker, L., …, Deoni, S.C.L., 2014a. Modeling healthy male white matter and myelin development: 3 through 60months of age. Neuroimage 84, 742–752. doi:10.1016/j.neuroimage.2013.09.058.

Dean, D.C, O'Muircheartaigh, J., Dirks, H., Waskiewicz, N., Walker, L., Doernberg, E., …, Deoni, S.C.L., 2014b. Characterizing longitudinal white matter development during early childhood. Brain Struct. Funct. 220 (4), 1921–1933. doi:10.1007/s00429-014-0763-3.

Deoni, S.C.L., O'Muircheartaigh, J., Elison, J.T., Walker, L., Doernberg, E., Waskiewicz, N., … Jumbe, N.L., 2014. White matter maturation profiles through early childhood predict general cognitive ability. Brain Struct. Funct. 221 (2), 1189–1203. doi:10.1007/s00429-014-0947-x.

Dimond, D., Rohr, C.S., Smith, R.E., Dhollander, T., Cho, I., Lebel, C., …, Bray, S., 2020. Early childhood development of white matter fiber density and morphology. Neuroimage 210, 116552. doi:10.1016/j.neuroimage.2020.116552.

Dubois, J., Dehaene-Lambertz, G., Perrin, M., Mangin, J.-.F., Cointepas, Y., Duchesnay, E., …, Hertz-Pannier, L., 2008. Asynchrony of the early maturation of white matter bundles in healthy infants: quantitative landmarks revealed noninvasively by diffusion tensor imaging. Hum. Brain Mapp. 29 (1), 14–27. doi:10.1002/hbm.20363.

Evans, G.W., 2006. Child development and the physical environment. Annu. Rev. Psychol. 57 (1), 423–451. doi:10.1146/annurev.psych.57.102904.190057.

Friedrich, P., Fraenz, C., Schlüter, C., Ocklenburg, S., Mädler, B., Güntürkün, O., Genç, E., 2020. The relationship between axon density, myelination, and fractional anisotropy in the human corpus callosum. Cereb. Cortex 30 (4), 2042–2056. doi:10.1093/cercor/bhz221.

Gao, W., Lin, W., Chen, Y., Gerig, G., Smith, J.K., Jewells, V., Gilmore, J.H., 2009. Temporal and spatial development of axonal maturation and myelination of white matter in the developing brain. AJNR Am. J. Neuroradiol. 30 (2), 290–296. doi:10.3174/ajnr.a1363.

Garyfallidis, E., Brett, M., Amirbekian, B., Rokem, A., Walt, S., van der, Descoteaux, M., …, Contributors, D., 2014. Dipy, a library for the analysis of diffusion MRI data. Front. Neuroinform. 8, 8. doi:10.3389/fninf.2014.00008.

Gee, D.G., Gabard-Durnam, L.J., Flannery, J., Goff, B., Humphreys, K.L., Telzer, E.H., …, Tottenham, N., 2013. Early developmental emergence of human amygdala-prefrontal connectivity after maternal deprivation. In: Proceedings of the National Academy of Sciences of the United States of America, 110, pp. 15638–15643. doi:10.1073/pnas.1307893110.

Geng, X., Gouttard, S., Sharma, A., Gu, H., Styner, M., Lin, W., …, Gilmore, J.H., 2012. Quantitative tract-based white matter development from birth to age 2years. Neuroimage 61 (3), 542–557. doi:10.1016/j.neuroimage.2012.03.057.

Genolini, C., Alacoque, X., Sentenac, M., Arnaud, C., 2015. kml and kml3d: R packages to cluster longitudinal data. J. Stat. Softw. 65 (1), 1–34. doi:10.18637/jss.v065.i04.

Giorgio, A., Watkins, K.E., Chadwick, M., James, S., Winmill, L., Douaud, G., …, James, A.C., 2010. Longitudinal changes in grey and white matter during adolescence. Neuroimage 49 (1), 94–103. doi:10.1016/j.neuroimage.2009.08.003.

Giorgio, A., Watkins, K.E., Douaud, G., James, A.C., James, S., Stefano, N.D., …, Johansen-

Berg, H., 2008. Changes in white matter microstructure during adolescence. Neuroimage 39 (1), 52–61. doi:10.1016/j.neuroimage.2007.07.043.

Girault, J.B., Cornea, E., Goldman, B.D., Knickmeyer, R.C., Styner, M., Gilmore, J.H., 2019. White matter microstructural development and cognitive ability in the first 2 years of life. Hum. Brain Mapp. 40 (4), 1195–1210. doi:10.1002/hbm.24439.

Hasegawa, M., Houdou, S., Mito, T., Takashima, S., Asanuma, K., Ohno, T., 1992. Development of myelination in the human fetal and infant cerebrum: a myelin basic protein immunohistochemical study. Brain Dev. 14 (1), 1–6. doi:10.1016/s0387-7604(12)80271-3.

Heng, S., Song, A.W., Sim, K., 2010. White matter abnormalities in bipolar disorder: insights from diffusion tensor imaging studies. J. Neural Transm. 117 (5), 639–654. doi:10.1007/s00702-010-0368-9.

Hermoye, L., Saint-Martin, C., Cosnard, G., Lee, S.-K., Kim, J., Nassogne, M.-C., …, Mori, S., 2006. Pediatric diffusion tensor imaging: normal database and observation of the white matter maturation in early childhood. Neuroimage 29 (2), 493–504. doi:10.1016/j.neuroimage.2005.08.017.

Howell, B.R., Ahn, M., Shi, Y., Godfrey, J.R., Hu, X., Zhu, H., …, Sanchez, M.M., 2019. Disentangling the effects of early caregiving experience and heritable factors on brain white matter development in rhesus monkeys. Neuroimage 197, 625–642. doi:10.1016/j.neuroimage.2019.04.013.

Huang, H., Zhang, J., Wakana, S., Zhang, W., Ren, T., Richards, L.J., …, Mori, S., 2006. White and gray matter development in human fetal, newborn and pediatric brains. Neuroimage 33 (1), 27–38. doi:10.1016/j.neuroimage.2006.06.009.

Jenkinson, M., Beckmann, C.F., Behrens, T.E.J., Woolrich, M.W., Smith, S.M, 2012. FSL. Neuroimage 62 (2), 782–790. doi:10.1016/j.neuroimage.2011.09.015.

Jones, D.K., Knösche, T.R., Turner, R., 2013. White matter integrity, fiber count, and other fallacies: the do's and don'ts of diffusion MRI. Neuroimage 73, 239–254. doi:10.1016/j.neuroimage.2012.06.081.

Kasprian, G., Brugger, P.C., Weber, M., Krssák, M., Krampl, E., Herold, C., Prayer, D., 2008. In utero tractography of fetal white matter development. Neuroimage 43 (2), 213–224. doi:10.1016/j.neuroimage.2008.07.026.

Kecskemeti, S., Samsonov, A., Hurley, S.A., Dean, D.C., Field, A., Alexander, A.L., 2015. MPnRAGE: a technique to simultaneously acquire hundreds of differently contrasted MPRAGE images with applications to quantitative T1 mapping. Magn. Reson. Med. 75 (3), 1040–1053. doi:10.1002/mrm.25674.

Kecskemeti, S., Samsonov, A., Velikina, J., Field, A.S., Turski, P., Rowley, H., …, Alexander, A.L., 2018. Robust motion correction strategy for structural MRI in unsedated children demonstrated with three-dimensional radial MPnRAGE. Radiology 289 (2), 509–516. doi:10.1148/radiol.2018180180.

Keunen, K., Counsell, S.J., Benders, M.J.N.L., 2017. The emergence of functional architecture during early brain development. Neuroimage 160, 2–14. doi:10.1016/j.neuroimage.2017.01.047.

Kim, J., Jung, Y., Barcus, R., Bachevalier, J.H., Sanchez, M.M., Nader, M.A., Whitlow, C.T., 2020. Rhesus macaque brain developmental trajectory: a longitudinal analysis using tensor-based structural morphometry and diffusion tensor imaging. Cereb. Cortex 30 (8), 4325–4335. doi:10.1093/cercor/bhaa015.

Kim, M.J., Whalen, P.J., 2009. The structural integrity of an amygdala-prefrontal pathway predicts trait anxiety. J. Neurosci. 29 (37), 11614–11618. doi:10.1523/jneurosci.2335-09.2009.

Kinney, H.C., Brody, B.A., Kloman, A.S., Gilles, F.H., 1988. Sequence of central nervous system myelination in human infancy. II. Patterns of myelination in autopsied infants. J. Neuropathol. Exp. Neurol. 47 (3), 217–234. doi:10.1097/00005072-198805000-00003.

Kinney, H.C., Karthigasan, J., Borenshteyn, N.I., Flax, J.D., Kirschner, D.A., 1994. Myelination in the developing human brain: biochemical correlates. Neurochem. Res. 19 (8), 983–996. doi:10.1007/bf00968708.

Kostovic, I., Rakic, P., 1980. Cytology and time of origin of interstitial neurons in the white matter in infant and adult human and monkey telencephalon. J. Neurocytol. 9 (2), 219–242. doi:10.1007/bf01205159.

Krogsrud, S.K., Fjell, A.M., Tamnes, C.K., Grydeland, H., Mork, L., Due-Tønnessen, P., …, Walhovd, K.B., 2016. Changes in white matter microstructure in the developing brain—A longitudinal diffusion tensor imaging study of children from 4 to 11years of age. Neuroimage 124 (Part A), 473–486. doi:10.1016/j.neuroimage.2015.09.017.

Kubicki, M., Baxi, M., Pasternak, O., Tang, Y., Karmacharya, S., Chunga, N., …, Rosene, D.L., 2019. Lifespan trajectories of white matter changes in rhesus monkeys. Cereb. Cortex (New York, N.Y. : 1991) doi:10.1093/cercor/bhy056.

Lebel, C., Beaulieu, C., 2011. Longitudinal development of human brain wiring continues from childhood into adulthood. J. Neurosci. 31 (30), 10937–10947. doi:10.1523/jneurosci.5302-10.2011.

Lebel, C., Walker, L., Leemans, A., Phillips, L., Beaulieu, C., 2008. Microstructural maturation of the human brain from childhood to adulthood. Neuroimage 40 (3), 1044–1055. doi:10.1016/j.neuroimage.2007.12.053.

Lebel, Catherine, Deoni, S., 2018. The development of brain white matter microstructure. Neuroimage 182, 207–218. doi:10.1016/j.neuroimage.2017.12.097.

Malkova, L., Heuer, E., Saunders, R.C., 2006. Longitudinal magnetic resonance imaging study of rhesus monkey brain development. Eur. J. Neurosci. 24 (11), 3204–3212. doi:10.1111/j.1460-9568.2006.05175.x.

Merisaari, H., Tuulari, J.J., Karlsson, L., Scheinin, N.M., Parkkola, R., Saunavaara, J., …, Karlsson, H., 2019. Test-retest reliability of diffusion tensor imaging metrics in neonates. Neuroimage 197, 598–607. doi:10.1016/j.neuroimage.2019.04.067.

Moura, L.M., Kempton, M., Barker, G., Salum, G., Gadelha, A., Pan, P.M., …, Jackowski, A.P., 2016. Age-effects in white matter using associated diffusion tensor imaging and magnetization transfer ratio during late childhood and early adolescence. Magn. Reson. Imaging 34 (4), 529–534. doi:10.1016/j.mri.2015.12.021.

Nelson, E.E., Winslow, J.T., 2009. Non-human primates: model animals for developmental psychopathology. Neuropsychopharmacology 34 (1), 90–105. doi:10.1038/npp.2008.150.

O'Muircheartaigh, J., Dean, D.C., Ginestet, C.E., Walker, L., Waskiewicz, N., Lehman, K., …, Deoni, S.C.L., 2014. White matter development and early cognition in babies and toddlers. Hum. Brain Mapp. 35 (9), 4475–4487. doi:10.1002/hbm.22488.

Phillips, K.A., Bales, K.L., Capitanio, J.P., Conley, A., Czoty, P.W., Hart, B.A.'t, …, Voytko, M.L., 2014. Why primate models matter. Am. J. Primatol. 76 (9), 801–827. doi:10.1002/ajp.22281.

Pierpaoli, C., Basser, P.J., 1996. Toward a quantitative assessment of diffusion anisotropy. Magn. Reson. Med. 36 (6), 893–906. doi:10.1002/mrm.1910360612.

Rakic, P., 1985. Limits of neurogenesis in primates. Science 227 (4690), 1054–1056. doi:10.1126/science.3975601.

Rakic, P., 1972. Mode of cell migration to the superficial layers of fetal monkey neocortex. J. Comp. Neurol. 145 (1), 61–83. doi:10.1002/cne.901450105.

Raschle, N., Zuk, J., Ortiz-Mantilla, S., Sliva, D.D., Franceschi, A., Grant, P.E., …, Gaab, N., 2012. Pediatric neuroimaging in early childhood and infancy: challenges and practical guidelines. Ann. N. Y. Acad. Sci. 1252 (1), 43–50. doi:10.1111/j.1749-6632.2012.06457.x.

Reynolds, J.E., Grohs, M.N., Dewey, D., Lebel, C., 2019. Global and regional white matter development in early childhood. Neuroimage 196, 49–58. doi:10.1016/j.neuroimage.2019.04.004.

Roberts, T.P.L., Liu, F., Kassner, A., Mori, S., Guha, A, 2005. Fiber density index correlates with reduced fractional anisotropy in white matter of patients with glioblastoma. AJNR Am. J. Neuroradiol. 26 (9), 2183–2186.

Sadeghi, N., Prastawa, M., Fletcher, P.T., Wolff, J., Gilmore, J.H., Gerig, G., 2013. Regional characterization of longitudinal DT-MRI to study white matter maturation of the early developing brain. Neuroimage 68, 236–247. doi:10.1016/j.neuroimage.2012.11.040.

Savadjiev, P., Whitford, T.J., Hough, M.E., Hohenberg, C.C.von, Bouix, S., Westin, C.-F., …, Kubicki, M., 2014. Sexually dimorphic white matter geometry abnormalities in adolescent onset schizophrenia. Cereb. Cortex 24 (5), 1389–1396. doi:10.1093/cercor/bhs422.

Scherf, K.S., Thomas, C., Doyle, J., Behrmann, M., 2014. Emerging structure–function relations in the developing face processing system. Cereb. Cortex 24 (11), 2964–2980. doi:10.1093/cercor/bht152.

Scott, J.A., Grayson, D., Fletcher, E., Lee, A., Bauman, M.D., Schumann, C.M., …, Amaral, D.G., 2015. Longitudinal analysis of the developing rhesus monkey brain using magnetic resonance imaging: birth to adulthood. Brain Struct. Funct. 221 (5), 2847–2871. doi:10.1007/s00429-015-1076-x.

Shi, Y., Short, S.J., Knickmeyer, R.C., Wang, J., Coe, C.L., Niethammer, M., …, Styner, M.A., 2013. Diffusion tensor imaging-based characterization of brain neurodevelopment in primates. Cereb. Cortex (New York, N.Y. : 1991) 23 (1), 36–48. doi:10.1093/cercor/bhr372.

Simmonds, D.J., Hallquist, M.N., Asato, M., Luna, B., 2014. Developmental stages and sex differences of white matter and behavioral development through adolescence: a longitudinal diffusion tensor imaging (DTI) study. Neuroimage 92 (C), 356–368. doi:10.1016/j.neuroimage.2013.12.044.

Telzer, E.H., Goldenberg, D., Fuligni, A.J., Lieberman, M.D., Gálvan, A., 2015. Sleep variability in adolescence is associated with altered brain development. Dev. Cognit. Neurosci. 14, 16–22. doi:10.1016/j.dcn.2015.05.007.

Tigges, Johannes, Gordon, Thomas, McClure, Harold, Hall, Elmer, Peters, Alan, 1988. Survival rate and life span of rhesus monkeys at the Yerkes regional primate research center. American Journal of Primatology 15 (3), 263–273. doi:10.1002/ajp.1350150308.

Tournier, J.-D., Smith, R., Raffelt, D., Tabbara, R., Dhollander, T., Pietsch, M., …, Connelly, A., 2019. MRtrix3: a fast, flexible and open software framework for medical image processing and visualisation. Neuroimage 202, 116137. doi:10.1016/j.neuroimage.2019.116137.

Tromp, D.P.M., Williams, L.E., Fox, A.S., Oler, J.A., Roseboom, P.H., Rogers, G.M., …, Kalin, N.H., 2019. Altered uncinate fasciculus microstructure in childhood anxiety disorders in boys but not girls. Am. J. Psychiatry 176 (3), 208–216. doi:10.1176/appi.ajp.2018.18040425.

Uda, S., Matsui, M., Tanaka, C., Uematsu, A., Miura, K., Kawana, I., Noguchi, K., 2015. Normal development of human brain white matter from infancy to early adulthood: a diffusion tensor imaging study. Dev. Neurosci. 37 (2), 182–194. doi:10.1159/000373885.

Workman, Alan, Charvet, Christine, Clancy, Barbara, Darlington, Richard, Finlay, Barbara, 2013. Modeling Transformations of Neurodevelopmental Sequences across Mammalian Species. Journal of Neuroscience 33 (17), 7368–7383. doi:10.1523/jneurosci.5746-12.2013.

Young, J.M., Morgan, B.R., Whyte, H.E.A., Lee, W., Smith, M.L., Raybaud, C., …, Taylor, M.J., 2017. Longitudinal study of white matter development and outcomes in children born very preterm. Cereb. Cortex doi:10.1093/cercor/bhw221.

Zakszewski, E., Adluru, N., Tromp, D.P.M., Kalin, N., Alexander, A.L, 2014. A diffusion-tensor-based white matter atlas for rhesus macaques. PLoS One 9 (9), e107398. doi:10.1371/journal.pone.0107398.

Zanin, E., Ranjeva, J., Confort-Gouny, S., Guye, M., Denis, D., Cozzone, P.J., Girard, N., 2011. White matter maturation of normal human fetal brain. An *in vivo* diffusion tensor tractography study. Brain Behav. 1 (2), 95–108. doi:10.1002/brb3.17.

Zhang, Y.P., Shi, L., 1993. Phylogeny of rheusus monkeys (Macaca mulatta) as revealed by mitochondrial DNA restriction enzyme analysis. Int. J. Primatol. 14 (4), 587–605. doi:10.1007/bf02215449.

Zhang, Y., Brady, M., Smith, S., 2001. Segmentation of brain Mr images through a hidden Markov random field model and the expectation-maximization algorithm. IEEE Trans. Med. Imaging 20 (1), 45. doi:10.1109/42.906424.